frontiers in Materials

ORIGINAL RESEARCH
published: 03 January 2022
doi: 10.3389/fmats.2021.813382

Formation and Anisotropic Mechanical Behavior of Stacking Fault Tetrahedron in Ni and CoCrFeNiMn High-Entropy Alloy

Sen Hu[1], Tao Fu[1,2], Qihao Liang[1], Shayuan Weng[1,2], Xiang Chen[3], Yinbo Zhao[4] and Xianghe Peng[1,2]**

[1]Department of Engineering Mechanics, Chongqing University, Chongqing, China, [2]State Key Laboratory of Coal Mine Disaster Dynamics and Control, Chongqing University, Chongqing, China, [3]Advanced Manufacturing Engineering, Chongqing University of Posts and Telecommunications, Chongqing, China, [4]Department of Aerospace Engineering, Tohoku University, Sendai, Japan

Stacking fault tetrahedron (SFT) is a kind of detrimental three-dimensional defect in conventional face-centered cubic (FCC) structural metals; however, its formation and anisotropic mechanical behavior in a CoCrFeNiMn high-entropy alloy (HEA) remain unclear. In this work, we first performed molecular dynamics simulations to verify the applicability of the Silcox-Hirsch mechanism in the CoCrFeNiMn HEA. The mechanical responses of the SFT to shear stress in different directions and that of the pure Ni counterpart were simulated, and the evolutions of the atomic structures of the SFTs during shear were analyzed in detail. Our results revealed that the evolution of the SFT has different patterns, including the annihilation of stacking faults, the formation and expansion of new stacking faults, and insignificant changes in stacking faults. It was found that the effects of SFT on the elastic properties of Ni and HEA are negligible. However, the introduction of SFT would reduce the critical stress, while the critical stress of the CoCrFeNiMn HEA is much less sensitive to SFT than that of Ni.

Keywords: stacking fault tetrahedron, CoCrFeNiMn high-entropy alloy, mechanical anisotropy, microstructural evolution, molecular dynamics

OPEN ACCESS

Edited by:
Jia Li,
Hunan University, China

Reviewed by:
Erqiang Liu,
Taiyuan University of Science and Technology, China
Fusheng Tan,
Hunan University, China

***Correspondence:**
Tao Fu
futaocqu@163.com
Xianghe Peng
xhpeng@cqu.edu.cn

Specialty section:
This article was submitted to Computational Materials Science, a section of the journal Frontiers in Materials

Received: *11 November 2021*
Accepted: *13 December 2021*
Published: *03 January 2022*

Citation:
Hu S, Fu T, Liang Q, Weng S, Chen X, Zhao Y and Peng X (2022) Formation and Anisotropic Mechanical Behavior of Stacking Fault Tetrahedron in Ni and CoCrFeNiMn High-Entropy Alloy. Front. Mater. 8:813382. doi: 10.3389/fmats.2021.813382

1 INTRODUCTION

The defects, including stacking fault tetrahedrons (SFTs), voids, dislocation loops, and bubbles, would be generated in metals subjected to long-term irradiation or severe deformation (Wu et al., 2018b; Wu et al., 2018c; Zhang et al., 2018; Chen et al., 2020). These defects would affect the mechanical properties of materials, such as irradiation hardening, swelling, embrittlement, and irradiation-assisted stress corrosion cracking (Bacon et al., 2009). The morphology and distribution of defects caused by irradiation depend on the lattice structure of materials and irradiation conditions. In face-centered cubic (FCC) metals, SFT is a kind of detrimental three-dimensional immobile defect (Singh et al., 2004; Wang et al., 2011a; Wang et al., 2011b; Wang et al., 2011c), which is predominantly generated from vacancy clusters (Kojima et al., 1991). In irradiated Cu, most SFTs are very small with the size of 2–3 nm but with a high density of about 1,022–1,024/m^3 (Kapinos et al., 1989; Fabritsiev and Pokrovsky, 2007).

SFT significantly affects the mechanical properties of materials (Matsukawa et al., 2005; Zhang et al., 2017a; Zhang et al., 2017b; Zhang et al., 2018). SFT can interact with dislocations and absorb

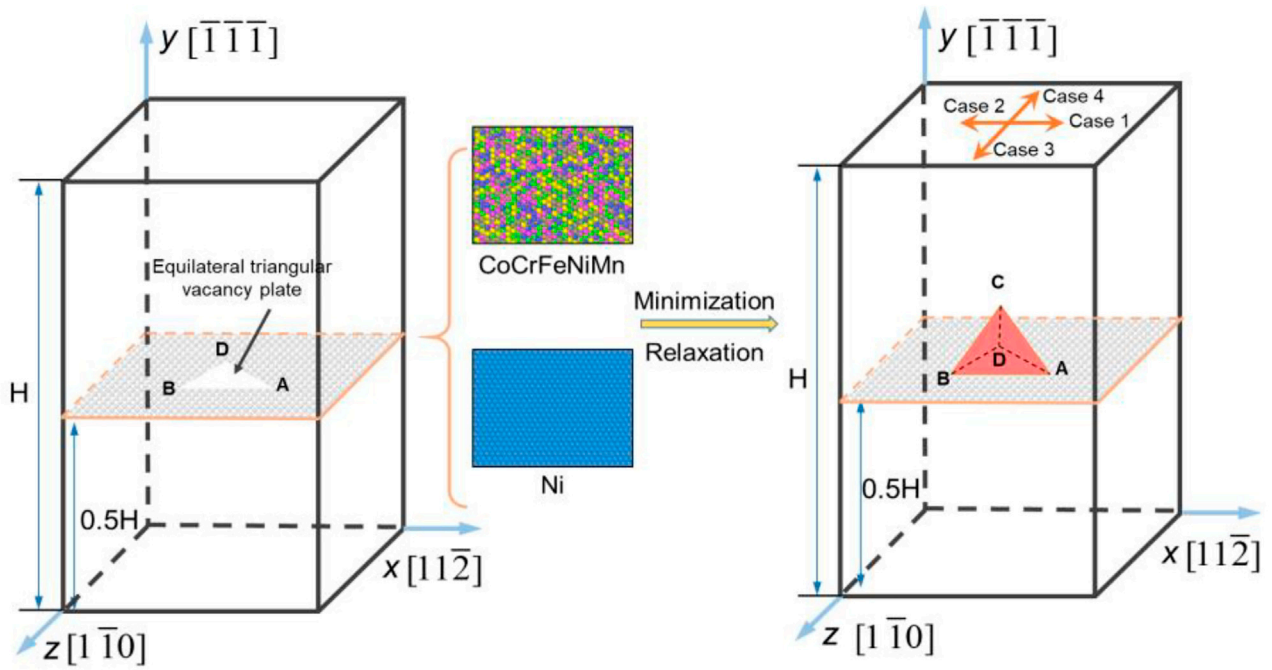

FIGURE 1 | Schematic illustration of the simulation process. Case 1 to Case 4 indicate that the shear directions are $(\bar{1}\bar{1}\bar{1})[11\bar{2}]$, $(\bar{1}\bar{1}\bar{1})[\bar{1}\bar{1}2]$, $(\bar{1}\bar{1}\bar{1})[1\bar{1}0]$, $(\bar{1}\bar{1}\bar{1})[\bar{1}10]$ of the samples, respectively. A, B, C and D are the four vertices of the SFT.

them, forming defect-free channels, in which dislocations can glide freely, resulting in the localization of plastic flow and loss of ductility (Robach et al., 2003; McMurtrey et al., 2014). Dai and Victoria (2011) proposed that the forming ability of SFT is closely related to the stacking fault energy (SFE): the lower the SFE, the easier the SFT is to form. High-entropy alloys (HEAs), as a new type of high-performance alloy, have attracted considerable attention due to their excellent mechanical properties and designability (Li et al., 2018; Feng et al., 2020; Luo et al., 2021; Peng et al., 2021; Ren et al., 2021). The SFEs of FCC HEAs are usually low (Huang et al., 2015; Chandan et al., 2021), and are even of negative values (Zhao et al., 2017), indicating that SFTs would form more easily in HEAs than in conventional alloys. CoCrFeNiMn is a kind of the most concerned FCC HEAs due to its excellent mechanical properties (Okamoto et al., 2016).

Based on the Silcox-Hirsch mechanism, SFTs can form after the aggregation of vacancies (Silcox and Hirsch, 1959a), generated under long-term irradiation or severe deformation in conventional metals. Despite the rapid development of experimental technology, it is still very challenging to study the evolution of SFTs under shear stress in different directions through experiments. Molecular dynamics (MD) simulations is an effective means to investigate the formation and evolution of microstructures under irradiation (Aidhy et al., 2015; Drouet et al., 2016; Dai et al., 2017; Zhu et al., 2017; Leino et al., 2018; Ke et al., 2019) and various mechanical loading (Weng et al., 2020; Chen et al., 2021; Weng et al., 2021), and the evolution of SFTs (Wu et al., 2018b; Wu et al., 2018c; Zhang et al., 2018; Chen et al., 2020). To study the formation and aggregation of vacancies using MD simulation of irradiation requires a long time and a lot of computing resources. Therefore, to study the effect of SFTs on the mechanical properties using MD simulations, SFTs are usually generated by minimizing and relaxing the system containing a planar triangular vacancy zone (Wu et al., 2017; Wu et al., 2018a; Wu et al., 2018b; Wu et al., 2018c). Based on the above considerations, we mainly focus on the process after the aggregation of vacancies to explore whether the Silcox-Hirsch formation mechanism of SFT applies to HEAs due to the severe lattice distortion caused by the multi-principal elements. If applicable, the effect of SFTs in HEAs on mechanical properties needs to be studied.

In this work, we use MD simulations to explore the following two questions: 1) the feasibility of the Silcox-Hirsch formation mechanism in HEAs, 2) the effect of SFT on the mechanical property of HEAs and the evolutions of SFTs under shear along different directions.

2 SIMULATION DETAILS

Figure 1 is the schematic illustration of the simulation process in this work. We first build pure Ni and CoCrFeNiMn HEA samples containing approximately 290,000 atoms, where the *x*, *y*, and *z* axes are parallel with $[11\bar{2}]$, $[\bar{1}\bar{1}\bar{1}]$, and $[1\bar{1}0]$, respectively, and the size is $13 \times 20 \times 12$ nm. At present, it is generally believed that the chemical short-range order (CSRO) is of great significance to the mechanical properties of HEAs. The abundant CSRO structures may affect the formation and evolution of SFT in HEAs. In this work, we only consider the random distribution of different types of atoms without considering the CSRO; therefore,

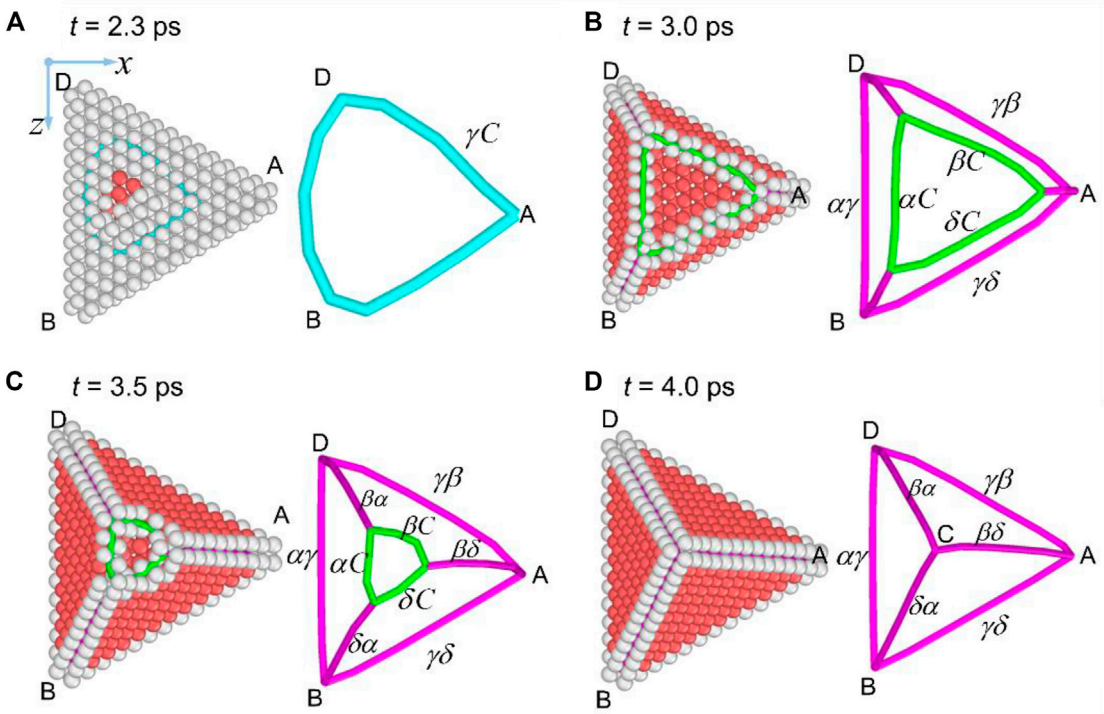

FIGURE 2 | Formation of SFT in CoCrFeNiMn. **(A)** Frank dislocation loop γC, **(B)** dissociation of Frank dislocations, **(C)** glide of Shockley partial dislocation, **(D)** perfect SFT, with red atoms representing SF.

five kinds of atoms (Co, Cr, Fe, Ni, Mn) are randomly distributed in a HEA sample. According to the current experimental results for FCC metals, the vacancies are usually distributed on the (111) plane, so an equilateral planar triangular vacancy zone is established on the (111) plane. Then, 91 atoms in the middle of the $(\overline{111})$ plane of the samples are removed to introduce an equilateral planar triangular vacancy zone; subsequently, energy minimization is carried out, followed by the relaxation at a given temperature. The energy minimization is performed by the conjugate gradient algorithm. The relaxation is performed for 40 ps under the NPT ensemble at a temperature of 300 K and a pressure of 0 bar (Rapaport, 1999), which leads to the formation of a SFT with an edge length of about 3 nm in the sample, within the range (2–4 nm) of SFTs in the irradiated metal Ni (Schäublin et al., 2006). The samples are then subjected to shear deformation in different directions with a strain rate of 1×10^9 s^{-1}, of which four shear directions, i.e., the positive and negative directions of the x and z axes, are adopted, indicated by Case 1 to Case 4, respectively. The stress components, except the one along the shear direction, are kept at zero during shear. For example, if the shear strain is imposed on the end of simulation box and along the x-axis direction, the pressure of the y-end and z-end is zero. In all the simulations, periodic boundary conditions are applied in all the three directions.

The second nearest-neighbor modified embedded-atom method (2NN MEAM) potential and the parameters developed by Choi et al. (2018) are employed to describe the interaction between the atoms, which have been widely used in the MD simulation of mechanical behaviors of CoCrFeNiMn HEA (Fang et al., 2019; Lee et al., 2021; Wang et al., 2021; Zhou et al., 2021). The stacking fault energy of CoCrFeNiMn calculated using these potential parameters is negative, consistent with first-principles calculation results (Zhao et al., 2017), which further demonstrates the validity of the potential. All simulations are carried out using the Large-scale Atomic/Molecular Massively Parallel Simulator (LAMMPS) (Plimpton, 1995).

Microstructures and deformation behaviors are analyzed with the adaptive common neighbor analysis (CNA) (Tsuzuki et al., 2007), dislocation extraction analysis (DXA) (Stukowski and Albe, 2010), and visualized using OVITO (Stukowski, 2010). The Burgers vector of dislocation, slip direction and slip plane are described using the Thompson tetrahedral notation (Silcox and Hirsch, 1959b; Wu et al., 2017).

3 RESULTS AND ANALYSES

3.1 Applicability of Silcox-Hirsch Mechanism in HEAs

Figure 2 shows the formation of a perfect SFT in CoCrFeNiMn from an equilateral planar triangle vacancy zone, which can be divided into four steps:

1) At t = 2.3 ps, the distances between the atoms on the upper and lower the planar triangular vacancy zone becomes smaller, forming a triangular Frank dislocation loop, whose

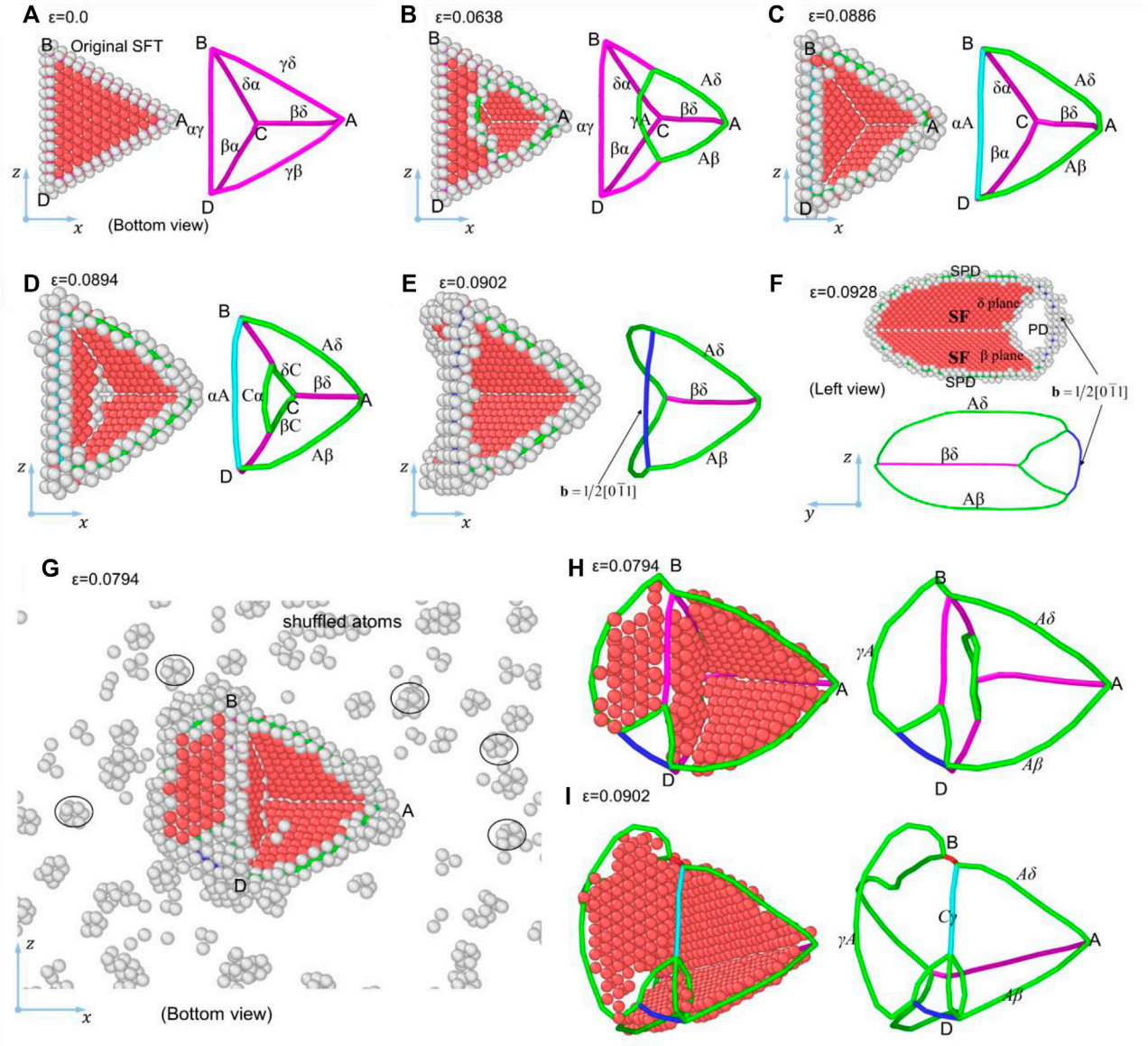

FIGURE 3 | Atomic structure of SFTs in Ni and CoCrFeNiMn samples sheared along $(\overline{111})[11\overline{2}]$ at different strains. **(A–F)** Ni; **(G–I)** CoCrFeNiMn HEA.

three edges are dislocations γC, as shown in **Figure 2A**. The stacking sequence of the triangular area along the y-axis is ***ABCBC***; therefore, this triangular area is an intrinsic stacking fault (SF).

2) The Frank dislocation loop γC is dissociated on different planes as follows,
   On the α plane: $\gamma C(\alpha) \rightarrow \gamma\alpha + \alpha C$
   On the β plane: $\gamma C(\beta) \rightarrow \gamma\beta + \beta C$
   On the δ plane: $\gamma C(\delta) \rightarrow \gamma\delta + \delta C$.

Therefore, three stair-rod dislocations (SRDs), $\gamma\alpha$, $\gamma\beta$ and $\gamma\delta$, and three Shockley partial dislocations (SPDs), αC, βC and δC, are obtained, as shown in **Figure 2B**.

3) The SRDs and SPDs on the same slip plane repel each other due to the acute intersection angle between their Burgers vector, causing the glide of SPDs on their respective slip planes (α, β, and δ), as shown in **Figures 2B,C**.
4) At the same time, the SPDs on the three slip planes intersect in pairs, forming three SRDs ($\alpha\beta$, $\delta\beta$, and $\alpha\delta$) as follows:
   The intersection of α and β planes: $\alpha C + C\beta \rightarrow \alpha\beta$
   The intersection of δ and β planes: $\delta C + C\beta \rightarrow \delta\beta$
   The intersection of α and δ planes: $\alpha C + C\delta \rightarrow \alpha\delta$

Three SRDs $\alpha\beta$, $\delta\beta$, and $\alpha\delta$ are synthesized (**Figures 2B,C**), and finally, intersect at Point C (**Figure 2D**). At this point, a

formation of a perfect SFT is finished, containing four SFs and six SRDs. The above process agrees with the Silcox-Hirsch formation mechanism of SFT in traditional metals, indicating that this mechanism is also applicable in FCC HEAs.

3.2 Transformation of SFT

3.2.1 Case 1 $(\overline{1}\overline{1}1)[11\overline{2}]$

Figures 3A–F show the atomic structure of the SFT in Ni sample sheared along $(\overline{1}\overline{1}1)[11\overline{2}]$ at the different strains, where the atoms identified as FCC have been removed for clarity and the rest atoms colored in red, blue, and gray correspond to HCP, BCC, and "other" structures, respectively. **Figures 3A–E** are the bottom views, and **Figure 3F** is the left view. **Figure 3A** shows the microstructure of a SFT at $\varepsilon = 0$, where the SFT is composed of six SRDs. Corresponding to the bottom plane ABD of the SFT, C is the vertex, and BD of the SFT is parallel with the *z*-axis. With the increase of ε, the evolution of the SFT can be divided into the following three stages:

1) Annihilation of the SF on the γ plane. With the increase of ε, two SRDs ($\gamma\delta$ and $\gamma\beta$) near Point A are dissociated into three SPDs (γA, $A\delta$, and $A\beta$) at $\varepsilon = 0.0638$, by $\gamma\delta \rightarrow \gamma A + A\delta$, $\gamma\beta \rightarrow \gamma A + A\beta$. Then, the dislocation γA glide on the γ plane in a bow shape, resulting in the annihilation of the SF on the γ plane, as shown in **Figure 3B**. When the dislocation γA meets and reacts with the SRD $\alpha\gamma$, forming a Frank partial dislocation (FPD) αA ($\alpha\gamma + \gamma A \rightarrow \alpha A$). At this time, the SF on the γ plane annihilates entirely, and the FPD αA generated remains parallel with the *z*-axis, as shown in **Figure 3C**.
2) Annihilation of the SF on the α plane. At $\varepsilon = 0.0886$, two SRDs ($\delta\alpha$ and $\beta\alpha$) near Point C are dissociated into three SPDs ($C\alpha$, δC and βC). Before the reaction of the dislocations on the α plane, the basal plane (γ) of the SFT has annihilated. Then, SPD $C\alpha$ glides on α plane, and the SF on α plane annihilates gradually, as shown in **Figure 3D**, which is similar to the annihilation of the SF on γ plane. At $\varepsilon = 0.0902$, SPD $C\alpha$ reacts with FPD αA, forming a perfect dislocation CA with Burgers vector of $1/2[0\overline{1}1]$, as shown in **Figure 3E**. The dislocation reactions can be expressed as $\delta\alpha \rightarrow \delta C + C\alpha$, $\beta\alpha \rightarrow \beta C + C\alpha$ and $C\alpha + \alpha A \rightarrow CA$.
3) Expansion of SFs on the δ and β planes. After the above two stages, the SFs on γ and α planes annihilate entirely, leaving two enlarged SFs on the δ and β planes. With the increase of strain, the ends of the perfect dislocation CA are pinned, but the SPDs on δ and β planes continue to glide on their slip planes, contributing to the expansion of the SFs on the δ and β planes. Eventually, it evolves into a structure where two SFs intersect at 60°, as shown in **Figure 3F**.

Figures 3G–I show the atomic structure of the SFT in the CoCrFeNiMn sample under shear along $(\overline{1}\overline{1}1)[11\overline{2}]$ at different strains, where the atoms identified as FCC have been removed for clarity. **Figure 3G** shows the atomic configuration at $\varepsilon = 0.0794$, where, in addition to the changes in SFT, there are some scattered white atoms far away from the SFT (often called shuffled atoms). To analyze the evolution of the SFT more clearly, these shuffled atoms and the other white atoms are also removed, as shown in **Figures 3H,I**. The microstructure evolution of the CoCrFeNiMn sample is similar to that of Ni, and the difference is that the SPD γA continues to glide and finally forms a SF on the γ plane. At $\varepsilon = 0.0794$, the SRDs $\gamma\beta$ and $\gamma\delta$ near Point A are dissociated into three SPDs, γA, $A\delta$, and $A\beta$. Then, γA glides on the γ plane, and the SF at the basal plane (γ plane) annihilates gradually, as shown in **Figure 3H**.

At $\varepsilon = 0.0902$, the SRDs $\delta\alpha$ and $\beta\alpha$ near Point C are dissociated into three SPDs, $C\alpha$, δC and βC, among which, $C\alpha$ glides on the α plane, and the SF on the α plane annihilates gradually. Afterward, $C\alpha$ meets with the SRD $\alpha\gamma$, generating an FPD $C\gamma$ ($C\alpha + \alpha\gamma \rightarrow C\gamma$), as shown in **Figure 3I**.

In this case, there are some differences between the response of CoCrFeNiMn and that of Ni. First, the reaction of γA on the basal plane with the SRD $\alpha\gamma$ of SFT does not generate Frank partial dislocation, but continues to slip forward, forming SFs on the left side of BD. Second, no dissociation of SRDs on the γ and α planes occurs. Third, there are more shuffled atoms in CoCrFeNiMn than in Ni.

3.2.2 Case 2 $(\overline{1}\overline{1}1)[\overline{1}\overline{1}2]$

The evolution of microstructures in the Ni sample sheared along $(\overline{1}\overline{1}1)[\overline{1}\overline{1}2]$ is different from that in Case 1. **Figures 4A–C** show the atomic structures of the SFT in the Ni sample sheared along $(\overline{1}\overline{1}1)[\overline{1}\overline{1}2]$ at different shear strains. At $\varepsilon = 0.1142$, two SRDs ($\delta\alpha$ and $\beta\alpha$) near Point C are dissociated into three SPDs ($C\alpha$, δC, and βC); subsequently, $C\alpha$ glides on its slip plane, forming a new SF. On the other hand, the original SFT tends to become smaller, which is different from the annihilation of SF in Case 1, as shown in **Figure 4A**. It indicates that the glide of SPDs can not only annihilate SFs but also form new SFs. The dissociation of the two SRDs ($\delta\alpha$ and $\beta\alpha$) near Point C follows $\delta\alpha \rightarrow \delta C + C\alpha$ and $\beta\alpha \rightarrow \beta C + C\alpha$.

After these reactions between dislocations and the further glide of dislocations, the SF on the α plane expands. Then a part of SPDs δC and βC react with SPDs $\gamma\delta$ and $\gamma\beta$ at Points B and D, forming two Frank dislocations γC, as shown in **Figure 4B**. The reactions can be expressed as, $\gamma\delta + \delta C \rightarrow \gamma C$ and $\gamma\beta + \beta C \rightarrow \gamma C$.

The above dislocation reaction shortens the dislocations δC and βC, leading to a reduction in the height of the SFT (from 15 atomic layers to 10 atomic layers). In general, the most critical microstructure evolution under shear along $(\overline{1}\overline{1}1)[\overline{1}\overline{1}2]$ is the formation of the SF on the α plane and the reduction of the SFT size, as shown in **Figure 4C**.

Figures 4D–G show the atomic structures of the SFT in CoCrFeNiMn under shear along $(\overline{1}\overline{1}1)[\overline{1}\overline{1}2]$ at different strains, where lots of shuffled atoms can be observed (**Figure 4D**). For clarity, the white atoms have been removed in **Figures 4E–G**. At $\varepsilon = 0.0728$, the SRD $\gamma\delta$ is dissociated into SPDs γA and $A\delta$, of which γA glides on the basal plane (ABD) of SFT, forming a SF, as shown in **Figure 4D**. At $\varepsilon = 0.0738$, the SRD $\gamma\beta$ is dissociated into SPDs γA and $A\beta$, of which the SPD γA glides on the basal plane (ABD), promoting the further expansion of the SF on the γ plane, as shown in **Figure 4E**. Then, the SRDs $\delta\alpha$ and $\beta\alpha$ on the α plane are also dissociated into SPDs δC, βC

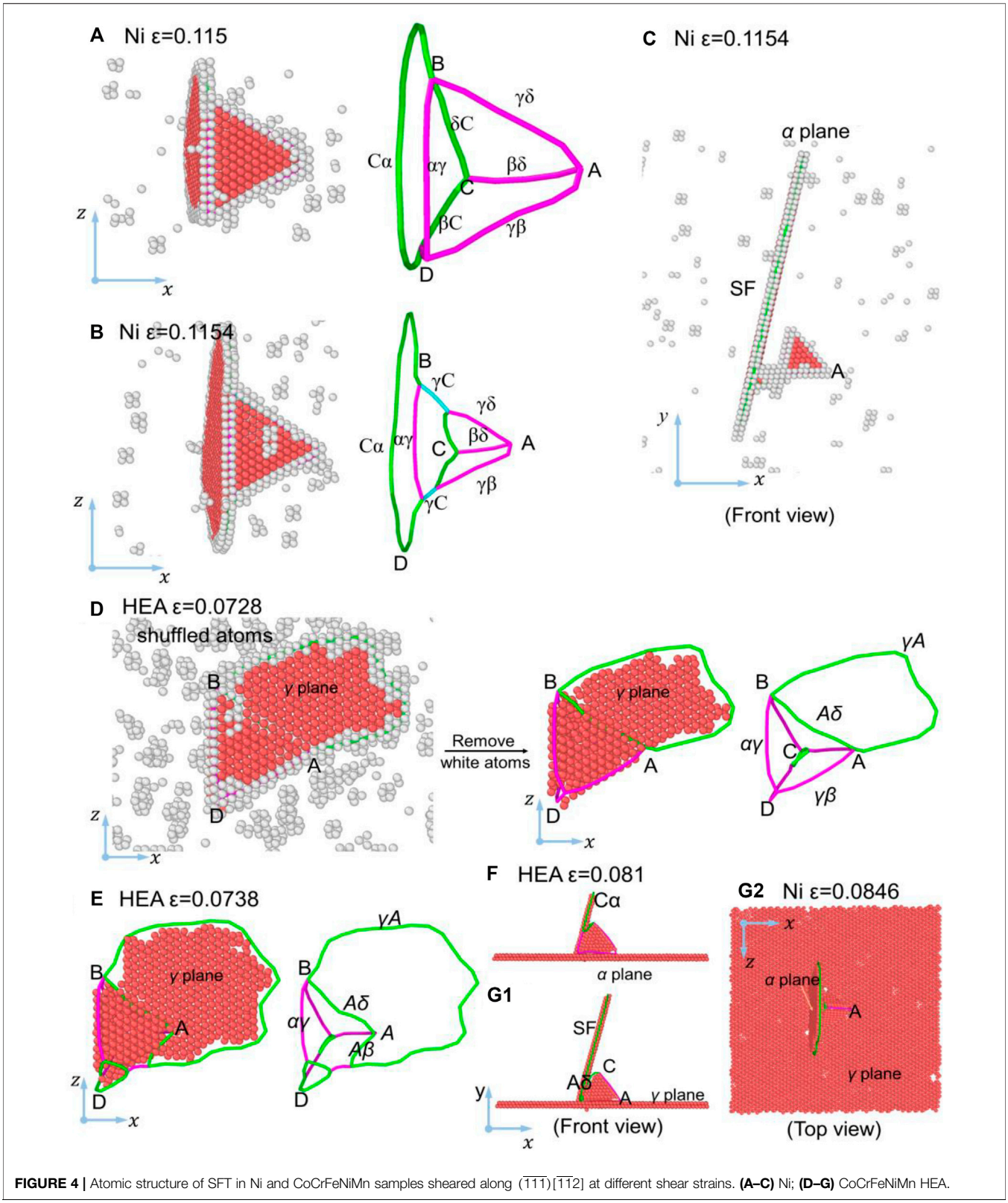

FIGURE 4 | Atomic structure of SFT in Ni and CoCrFeNiMn samples sheared along $(\overline{1}11)[\overline{1}\overline{1}2]$ at different shear strains. **(A–C)** Ni; **(D–G)** CoCrFeNiMn HEA.

and *Cα*. At $\varepsilon = 0.081$, the glide of the dislocation *Cα* forms a SF on the α plane (**Figure 4F**). Finally, the SFs on the γ and α planes form, and, compared with Ni, the most distinct difference is that a SF on the bottom plane forms firstly, before the formation of a SF on the α plane. The SF on the α plane stops when it meets with the SF on the γ plane, as shown in **Figure 4G**.

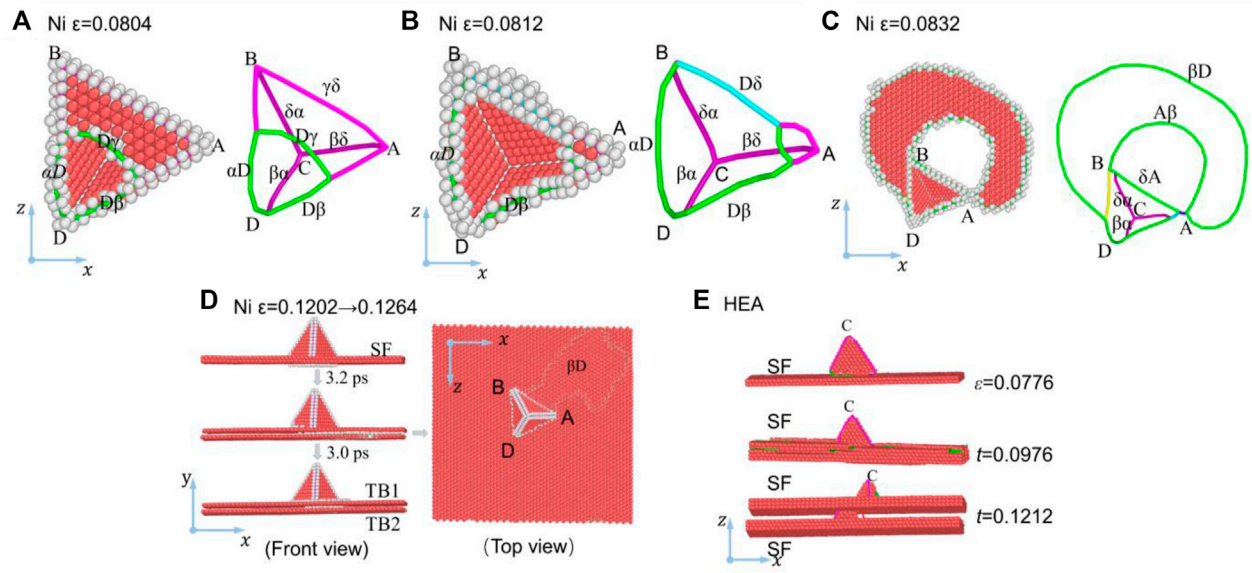

FIGURE 5 | Atomic structures of SFTs in Ni and CoCrFeNiMn samples sheared along $(\overline{1}11)[1\overline{1}0]$ at different shear strains. **(A–D)** Ni. **(E)** CoCrFeNiMn HEA.

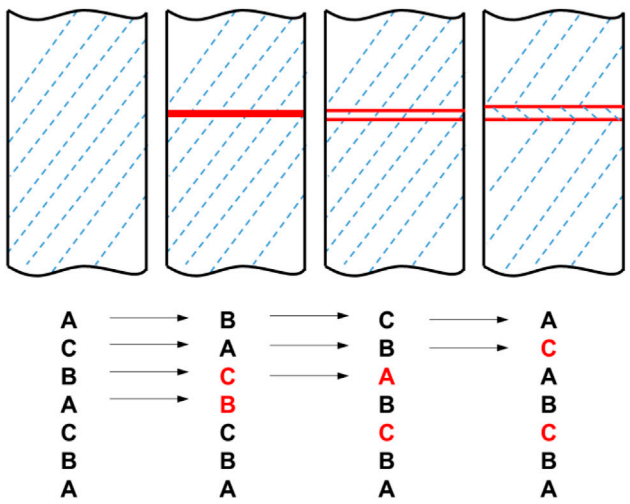

FIGURE 6 | Illustration for the formation of TBs.

3.2.3 Case 3 $(\overline{1}11)[1\overline{1}0]$

Figures 5A–D show the atomic structures of the SFT in the Ni sample sheared along $(\overline{1}11)[1\overline{1}0]$ at different shear strains. Like Case 1, SRDs are first dissociated into SPDs. At $\varepsilon = 0.0792$, two SRDs ($\alpha\gamma$ and $\gamma\beta$) are dissociated into three SPDs (αD, γD, and $D\beta$) from Point D on the γ plane ($\alpha\gamma \rightarrow \alpha D + D\gamma$, $\gamma\beta \rightarrow \gamma D + D\beta$). Then the γD (or $D\gamma$) glides on the γ plane, inducing the annihilation of a SF on the γ plane, as shown in **Figure 5A**.

With the increase of shear strain, the γD reacts with the $\delta\gamma$, forming an FPD δD ($\delta\gamma + \gamma D \rightarrow \delta D$), as shown in **Figure 5B**. Then the δD is dissociated into three SPDs δA, $A\beta$ and βD ($\delta D \rightarrow \delta A + A\beta + \beta D$). The βD and $A\beta$ glide on the γ plane, and their movement yields a stable SF, as shown in **Figure 5C**. Finally, a mixed plane of the SF and the twin boundary (TB) is observed on the γ plane of the SFT. It shows in **Figure 5D** that, as ε is increased from 0.1202 to 0.1264, the upper surface of the SF re-nucleates and generates an SPD βD by following the Orowan mechanism (Scattergood and Bacon, 1975). Then βD glides on the upper plane and eventually forms two twin boundaries (TB1 and TB2), which reduces the height of SFT from 15 atomic layers to 12 atomic layers.

The formation of TBs can be illustrated in **Figure 6**. A dislocation nucleates from the SFT and glides, forming a stacking fault, with the stacking sequence varying from ***ABCABCA*** … to ***ABCBCAB*** … Then, an SPD glides on the plane that is one atomic layer higher than the γ plane, resulting in an upward movement of the upper atomic layer of the SF and separating the two atomic layers in the SF structure. The stacking sequence varies from ***ABCBCAB*** … to ***ABCBABC*** … Subsequently, new SPD nucleates from the SFT and glides on a higher atomic plane, contributing to the upward movement of the upper atomic layer of the SF. Accordingly, the stacking sequence varies from ***ABCBABC*** … to ***ABCBACA*** … With the glide of the dislocation, the upper atomic layer of the SF moves upwards, increasing the spacing between the two atomic layers and the formation of two TBs. This evolution causes the upward movement of the bottom plane of the SFT, which reduces the SFT height.

Figure 5E shows the microstructures in CoCrFeNiMn under shear along $(\overline{1}11)[1\overline{1}0]$ at $\varepsilon = 0.0776$, 0.0976, and 0.1212. Similar to that in Ni, two SRDs are first dissociated into SPDs and then glide, inducing the annihilation of the SF on the γ plane. Then two SPDs glide on the γ plane of the SFT, resulting in a SF that replaces the bottom area of the SFT at $\varepsilon = 0.0776$. With the increase of shear strain, dislocations form on the SF, and the SF

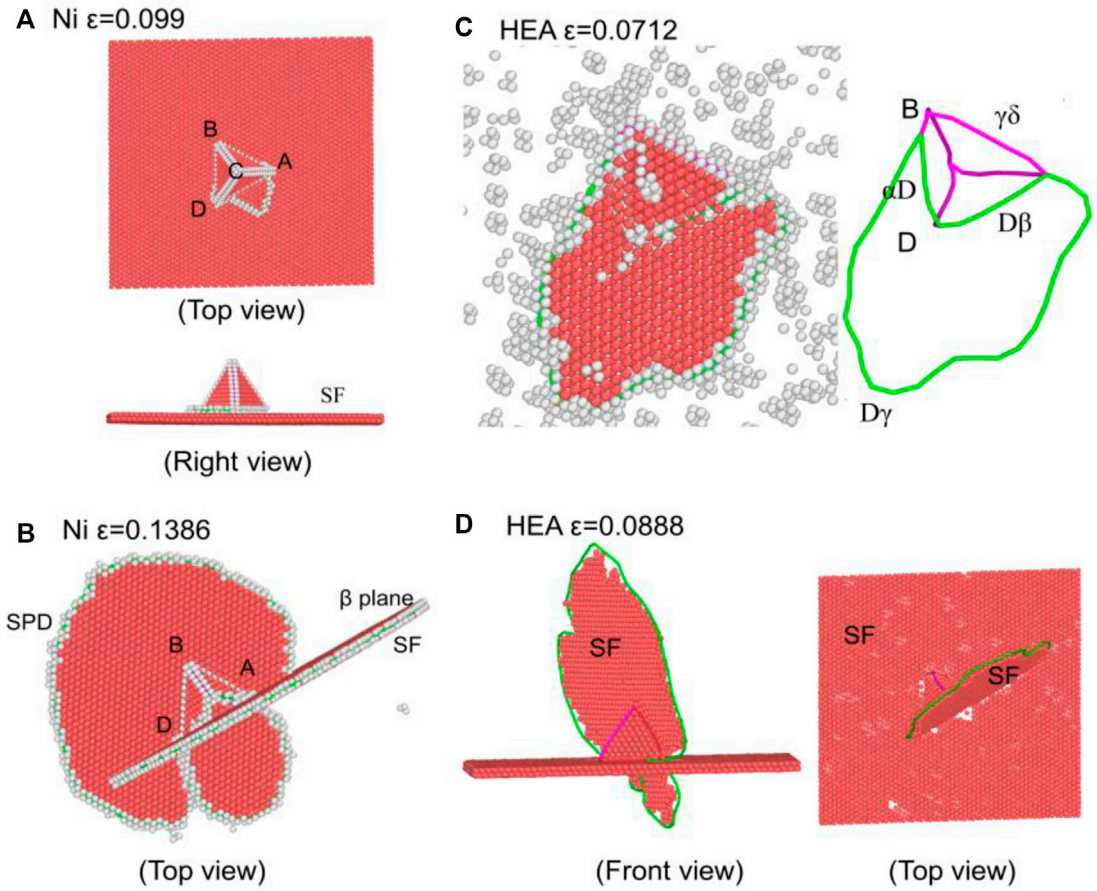

FIGURE 7 | Atomic structures of SFTs in Ni and CoCrFeNiMn samples sheared along $(\overline{1}11)[\overline{1}10]$ at different shear strains, **(A,B)** Ni. **(C,D)** CoCrFeNiMn HEA.

zone expands, forming a multiatomic layer (about five atomic layers) SF at the bottom of the SFT, which leads to the reduction in the height of the SFT, from 11 atomic layers at $\varepsilon = 0.0776$ to 8 atomic layers at $\varepsilon = 0.0976$. At $\varepsilon = 0.1212$, the middle part of the multiatomic layer SF annihilates, resulting in two SF zones, as shown in **Figure 5E**.

3.2.4 Case 4 $(\overline{1}11)[\overline{1}10]$

For Ni, the microstructural evolution in Case 4 is similar to that in Case 3, except that the SF forms on the β plane. At $\varepsilon = 0.0826$, the SRD near Point D is dissociated into three SPDs, αD, γD, and $D\beta$. Then, γD glides on the γ plane, yielding a SF at $\varepsilon = 0.099$, as shown in **Figure 7A**. Different from Case 3, the SRDs, $\beta\delta$ and $\beta\alpha$, near the vertex C, are dissociated into three SPDs, βC, $C\delta$ and $C\alpha$. The SPD βC glides on its slip plane, generating a new SF on the β plane, as shown in **Figure 7B**. The dissociation of $\beta\delta$ and $\beta\alpha$ can be expressed as $\beta\delta \rightarrow \beta C + C\delta$ and $\beta\alpha \rightarrow \beta C + C\alpha$.

Figures 7C,D show the atomic structures of the SFT in CoCrFeNiMn under shear along $(\overline{1}11)[\overline{1}10]$, where lots of shuffled atoms can be observed (**Figure 7C**). The response of the CoCrFeNiMn is similar to that of Ni. With the increase of shear strain, the evolution of the SFT can be divided into two stages: 1) the formation and expansion of the SFs on the γ plane; 2) the formation of SFs on the β plane. The difference in the case of Ni is that when SFs form, γD does not glide on the γ plane, but glides outside the bottom surface of the SFT (outside the γ plane), leading to a SF, as shown in **Figure 7D**, and the final result agrees with that in Ni, as shown in **Figure 7B**.

4 DISCUSSION

The shear stress-strain ($\sigma-\varepsilon$) curves of Ni and the CoCrFeNiMn HEA samples (each containing a SFT at its center) subjected to shear deformation in the four directions at 300 K are shown in **Figure 8A**. For comparison, the same shear simulations of Ni and the CoCrFeNiMn HEA samples without any SFT are performed, and the $\sigma-\varepsilon$ curves are shown in **Figure 8B**. The $\sigma-\varepsilon$ curves of Ni are higher than those of CoCrFeNiMn, which should be ascribed to the higher generalized stacking fault (GSF) energy curves of Ni (**Figure 8C**). For Ni and the HEA, the shear direction in Case 1 and Case 3 is opposite to that in Case 2 and Case 4, respectively. Therefore, for the Ni and HEA samples with or without a SFT, the $\sigma-\varepsilon$ curves in Case 1 are higher than those in Case 2, while those in Case 3 and Case 4 almost coincide, which could be attributed to the symmetry of atomic arrangement. From the GSF energy

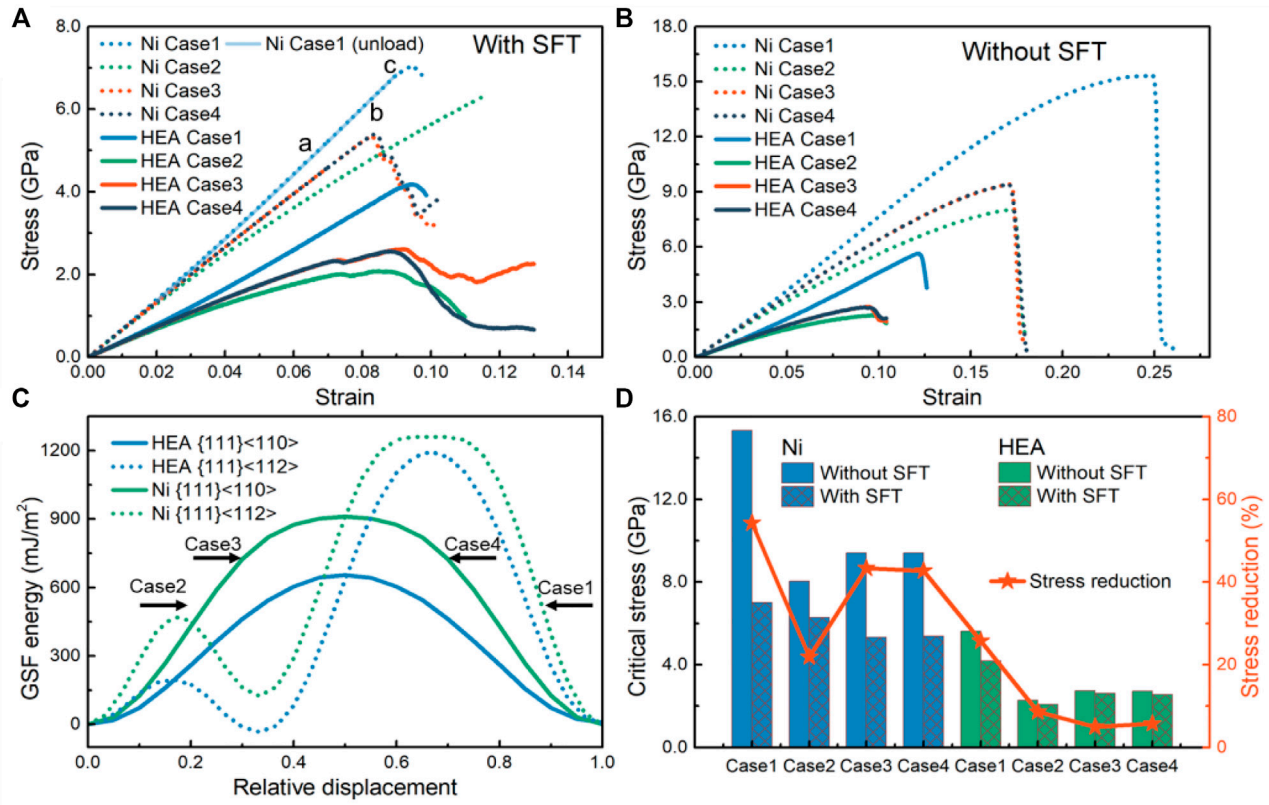

FIGURE 8 | Shear stress-strain curves of Ni and CoCrFeNiMn HEA samples sheared along four directions at 300 K. **(A)** with SFT; **(B)** without SFT; **(C)** Variations of GSF energies of different slip systems with relative displacement; **(D)** Comparison of critical shear stress between samples with and without SFT.

TABLE 1 | Shear moduli (G), critical shear stresses (τ_{max}), energy barriers (E_m) and incipient nucleation points of Ni and CoCrFeNiMn HEA samples with a SFT under shear along different directions. The results of samples without SFT are provided in brackets ( ) for comparison.

	Sample	Case 1 [$11\bar{2}$]	Case 2 [$\bar{1}\bar{1}2$]	Case 3 [$1\bar{1}0$]	Case 4 [$\bar{1}10$]
G (GPa)	Ni	70.75 (70.78)	63.54 (63.48)	66.86 (66.82)	66.88 (66.92)
	HEA	40.36 (40.07)	33.44 (33.56)	36.22 (36.4)	36.23 (36.27)
τ_{max} (GPa)	Ni	7.01 (15.33)	6.28 (8.05)	5.33 (9.41)	5.39 (9.41)
	HEA	4.18 (5.63)	2.08 (2.28)	2.61 (2.75)	2.57 (2.72)
E_m (mJ/m^2)	Ni	1,260.0	472.8	910.3	910.3
	HEA	1,195.5	196.8	655.2	655.2
Incipient nucleation point	Ni	A	C	D	D
	HEA	A	C	D	D

curves in **Figure 8C**, one can see that the curves of (111)<110> are bilaterally symmetric, i.e., the curves from the relative displacement from 0.0 to 1.0 (Case 3) are equivalent to those from the relative displacement from 1.0 to 0.0 (Case 4); while the curves of (111)<112> are asymmetrical, indicating that gliding in Case 2 is much easier than that in Case 1. Therefore, Case 2 and Case 1 are usually referred to as "Easy" and "Hard" slip direction, respectively (Li et al., 2014; Li et al., 2016; Yang et al., 2019). The shear modulus G can be obtained by fitting the slope of these curves at the initial stage, as listed in **Table 1**, where it can be seen that the shear moduli of the samples with SFT are consistent with that of samples without SFT for both Ni and HEA, indicating that SFT has a negligible effect on the G.

The energy barrier E_m is usually used to predict the slip order; the higher the energy barrier, the more difficult the glide (Yadav et al., 2014; Fu et al., 2015a; Fu et al., 2015b). For the Ni and CoCrFeNiMn samples without SFT, the relationship of critical shear stress τ of the four cases is $\tau_{Case1} > \tau_{Case3} \approx \tau_{Case4} > \tau_{Case2}$, following the relationship of energy barriers (**Table 1**). The energy barriers of Case 3 and Case 4 are about two to three times that of Case 2; however, τ_{Case3} and τ_{Case4} are only about 20%

TABLE 2 | Final states of SFTs and characteristics of dislocation lines in Ni and CoCrFeNiMn HEA samples sheared in different directions. Annihilation denoting annihilation of SF; Expansion, formation and expansion of new SF; invariance, insignificant changes in stacking faults.

	Materials	α	β	Γ	δ	Dislocation lines
Case 1	Ni	Annihilation	Expansion	Annihilation	Expansion	Smooth
	HEA	Annihilation	Expansion	Expansion	Expansion	Tortuous
Case 2	Ni	Expansion	Invariance	Invariance	Invariance	Smooth
	HEA	Expansion	Invariance	Expansion	Invariance	Tortuous
Case 3	Ni	Invariance	Invariance	Expansion	Invariance	Smooth
	HEA	Invariance	Invariance	Expansion	Invariance	Tortuous
Case 4	Ni	Invariance	Expansion	Expansion	Invariance	Smooth
	HEA	Invariance	Expansion	Expansion	Invariance	Tortuous

higher than that of Case 2. Despite the shear along the <110> direction (Case 3 and Case 4), the deformation mechanism is also the nucleation and slip of partial dislocations; therefore, τ_{Case3} and τ_{Case4} are moderately larger than τ_{Case2}. For the samples with SFT, the maximum stresses show different relationships: for Ni, $\tau_{Case\ 1} > \tau_{Case\ 2} > \tau_{Case\ 3} \approx \tau_{Case\ 4}$, following the relationship of energy barrier, but for CoCrFeNiMn, $\tau_{Case\ 1} > \tau_{Case\ 3} \approx \tau_{Case\ 4} > \tau_{Case\ 2}$, which does not follow the relationship of energy barriers.

Since the maximum stress here does not correspond to dislocation nucleation and the annihilation of the γ plane does not lead to a drop in stress, the sudden drop in stress should correspond to plastic deformation. For example, in Case 1 for Ni, the microstructures at Points "a" and "b" in **Figure 8A** correspond to the dissociation of SRDs and the annihilation of the SF on the α plane (**Figures 3B,D**), but the shear stress remains increasing, and the crystal is in the initial stage of plastic deformation. Then, the glide of SPD induces the SFs on the δ and β planes, resulting in a drop in stress. To further explore the response of the annihilation of SF on the γ plane to the stress, we perform an unloading simulation from ε = 0.092 (Point "c" in **Figure 8A**), and found that the SFT returns to its original shape. It can be speculated that the energy stored in the material could provide the energy required for the recovery. In Case 2 for Ni, the formation of the SFs on the α plane causes the drop in stress, while in Case 3 and Case 4, the annihilation of the SF on the γ plane induces the drop in stress.

Figure 8D shows the comparison of critical shear stress between the samples containing SFT with those without containing SFT, where one can see that the introduction of SFT would reduce the mechanical properties of both Ni and the HEA. However, the stress reduction caused by SFT in the HEA for each case is much less than that in Ni, showing that the mechanical properties of the HEA are less dependent on SFT. This weaker dependence may be attributed to the self-adjustment of the internal stress due to the multi-component nature of HEA.

During shear, besides the slip and evolution of dislocations, there are some atoms that are far from their equilibrium positions and are identified as shuffled atoms. These shuffled atoms can only be observed in the Ni sample in Case 2, but can be observed commonly in the CoCrFeNiMn samples subjected to shear along different directions, which could be ascribed to the lattice distortion effect.

The dislocation nucleation points in the Ni and CoCrFeNiMn HEA samples subjected to shear deformation along different directions are summarized and shown in **Table 1**. The positions of incipient nucleation of dislocations are all from the three vertices of the SFTs (A, C and D in **Figure 1**). Dislocation nucleates from Point A in Case 1; from Point C in Case 2; and from Point D in Case 3 and Case 4, indicating that the site of incipient nucleation of dislocations is related to the shear direction.

The microstructures in Ni and the CoCrFeNiMn HEA are versatile in different cases, but the primary evolutions are all around the four planes of the SFT (α, β, δ, γ), including the annihilation of SF (Annihilation) and formation and expansion of new SFs (Expansion) and insignificant changes of SFs (Invariance), as summarized in **Table 2**. On the α, β and δ planes, no significant differences can be detected between Ni and CoCrFeNiMn for each case; but on the γ plane, there are distinct differences between Ni and CoCrFeNiMn for both Case 1 and Case 2. In the CoCrFeNiMn sample, a new SF forms; while in Ni, the SF annihilates and keeps invariant in Case 1 and Case 2, respectively. Another essential difference of the microstructures in Ni with that in the CoCrFeNiMn HEA is that the dislocation lines in Ni are smooth, while that in the HEA are more tortuous, which can also be attributed to the multi-component feature.

5 CONCLUSION

In this work, the energy minimization and relaxation for the Ni and CoCrFeNiMn high-entropy alloy (HEA) samples containing an equilateral planar triangular vacancy zone were simulated with molecular dynamics (MD), aiming to verify the applicability of the Silcox-Hirsch mechanism in the formation of stacking fault tetrahedrons (SFTs) in CoCrFeNiMn HEAs. Then, the mechanical responses of the SFTs in the Ni and HEA samples subjected to shear deformation along different directions, as well as the evolutions of their atomic structures, were studied comparatively in detail. It was shown that the evolutions of the SFTs have various patterns, including the annihilation of stacking faults, formation and expansion of new stacking faults, and insignificant changes in stacking faults. The effects of SFT on the elastic properties of Ni and HEA are negligible.

However, the introduction of SFT would reduce the critical stress in both Ni and the HEA, but the reduction in the HEA is much smaller than that in Ni. It was also found that the site of incipient nucleation of dislocations is related to the shear direction.

It should be noted that the chemical short-range order may be of great significance to the formation and evolution of stacking fault tetrahedrons, which requires hybrid MD and Monte Carlo simulations to obtain HEAs with optimized chemical short-range order.

DATA AVAILABILITY STATEMENT

The original contributions presented in the study are included in the article/Supplementary Material, further inquiries can be directed to the corresponding authors.

AUTHOR CONTRIBUTIONS

SH, SW, and TF designed the scheme and wrote the manuscript under the guidance of XP. SH, QL, and TF performed the calculations and analyzed the results. YZ and XC participated in the discussions and provided valuable suggestions. All authors contributed to the manuscript, read and approved the submitted version.

FUNDING

This work is supported by the National Natural Science Foundation of China (Nos 11932004, 11802045, and 11802047) and the Chongqing Natural Science Foundation (No. cstc2019jcyj-bshX0029). This work was performed at Lv Liang Cloud Computing Center of China, and the calculations were performed on TianHe-2.

REFERENCES

Aidhy, D. S., Lu, C., Jin, K., Bei, H., Zhang, Y., Wang, L., et al. (2015). Point Defect Evolution in Ni, NiFe and NiCr Alloys from Atomistic Simulations and Irradiation Experiments. *Acta Mater.* 99, 69–76. doi:10.1016/j.actamat.2015.08.007

Bacon, D. J., Osetsky, Y. N., and Rodney, D. (2009). "Chapter 88 Dislocation-Obstacle Interactions at the Atomic Level," in *Dislocations in Solids*. Editor J. P. H. Kubin (Amsterdam, Netherlands: Elsevier), 1–90. doi:10.1016/s1572-4859(09)01501-0

Chandan, A. K., Tripathy, S., Sen, B., Ghosh, M., and Ghosh Chowdhury, S. (2021). Temperature Dependent Deformation Behavior and Stacking Fault Energy of Fe40Mn40Co10Cr10 alloy. *Scr. Mater.* 199, 113891. doi:10.1016/j.scriptamat.2021.113891

Chen, X., He, X., Chen, Y., Jia, L., Yang, W., Hu, W., et al. (2020). Molecular Dynamics Simulation of the Interactions between Screw Dislocation and Stacking Fault Tetrahedron in Fe-10Ni-20Cr and Ni. *Model. Simul. Mater. Sci. Eng.* 28, 075002. doi:10.1088/1361-651x/abac50

Chen, X., Weng, S., Yue, X., Fu, T., and Peng, X. (2021). Effects of Anisotropy and In-Plane Grain Boundary in Cu/Pd Multilayered Films with Cube-On-Cube and Twinned Interface. *Nanoscale Res. Lett.* 16, 69. doi:10.1186/s11671-021-03528-9

Choi, W.-M., Jo, Y. H., Sohn, S. S., Lee, S., and Lee, B.-J. (2018). Understanding the Physical Metallurgy of the CoCrFeMnNi High-Entropy alloy: an Atomistic Simulation Study. *Npj Comput. Mater.* 4, 1. doi:10.1038/s41524-017-0060-9

Dai, Y., and Victoria, M. (2011). Defect Cluster Structure and Tensile Properties of Copper Single Crystals Irradiated with 600 MeV Protons. *MRS Proc.* 439, 319. doi:10.1557/proc-439-319

Dai, C., Saidi, P., Yao, Z., and Daymond, M. R. (2017). Atomistic Simulations of Ni Segregation to Irradiation Induced Dislocation Loops in Zr-Ni Alloys. *Acta Mater.* 140, 56–66. doi:10.1016/j.actamat.2017.08.016

Drouet, J., Dupuy, L., Onimus, F., and Mompiou, F. (2016). A Direct Comparison between *In-Situ* Transmission Electron Microscopy Observations and Dislocation Dynamics Simulations of Interaction between Dislocation and Irradiation Induced Loop in a Zirconium alloy. *Scr. Mater.* 119, 71–75. doi:10.1016/j.scriptamat.2016.03.029

Fabritsiev, S. A., and Pokrovsky, A. S. (2007). Effect of Irradiation Temperature on Microstructure, Radiation Hardening and Embrittlement of Pure Copper and Copper-Based alloy. *J. Nucl. Mater.* 367-370, 977–983. doi:10.1016/j.jnucmat.2007.03.056

Fang, Q., Chen, Y., Li, J., Jiang, C., Liu, B., Liu, Y., et al. (2019). Probing the Phase Transformation and Dislocation Evolution in Dual-phase High-Entropy Alloys. *Int. J. Plast.* 114, 161–173. doi:10.1016/j.ijplas.2018.10.014

Feng, H., Cui, S., Chen, H., Song, X., Fang, Q., Li, J., et al. (2020). A Molecular Dynamics Investigation into Deformation Mechanism of Nanotwinned Cu/high Entropy alloy FeCoCrNi Nanolaminates. *Surf. Coat. Techn.* 401, 126325. doi:10.1016/j.surfcoat.2020.126325

Fu, T., Peng, X., Huang, C., Yin, D., Li, Q., and Wang, Z. (2015a). Molecular Dynamics Simulation of VN Thin Films under Indentation. *Appl. Surf. Sci.* 357, 643–650. doi:10.1016/j.apsusc.2015.09.024

Fu, T., Peng, X., Zhao, Y., Sun, R., Yin, D., Hu, N., et al. (2015b). Molecular Dynamics Simulation of the Slip Systems in VN. *RSC Adv.* 5, 77831–77838. doi:10.1039/c5ra15878h

Huang, S., Li, W., Lu, S., Tian, F., Shen, J., Holmström, E., et al. (2015). Temperature Dependent Stacking Fault Energy of FeCrCoNiMn High Entropy alloy. *Scr. Mater.* 108, 44–47. doi:10.1016/j.scriptamat.2015.05.041

Kapinos, V. G., Osetskii, Y. N., and Platonov, P. A. (1989). The cascade Mechanism of Nucleation of Vacancy Loops and Stacking Fault Tetrahedra in FCC Metals. *J. Nucl. Mater.* 165, 286–296. doi:10.1016/0022-3115(89)90206-7

Ke, J.-H., Reese, E. R., Marquis, E. A., Odette, G. R., and Morgan, D. (2019). Flux Effects in Precipitation under Irradiation - Simulation of Fe-Cr Alloys. *Acta Mater.* 164, 586–601. doi:10.1016/j.actamat.2018.10.063

Kojima, S., Zinkle, S. J., and Heinisch, H. L. (1991). Radiation Hardening in Neutron-Irradiated Polycrystalline Copper: Barrier Strength of Defect Clusters. *J. Nucl. Mater.* 179-181, 982–985. doi:10.1016/0022-3115(91)90255-6

Lee, H., Shabani, M., Pataky, G. J., and Abdeljawad, F. (2021). Tensile Deformation Behavior of Twist Grain Boundaries in CoCrFeMnNi High Entropy alloy Bicrystals. *Sci. Rep.* 11, 428. doi:10.1038/s41598-020-77487-z

Leino, A. A., Samolyuk, G. D., Sachan, R., Granberg, F., Weber, W. J., Bei, H., et al. (2018). GeV Ion Irradiation of NiFe and NiCo: Insights from MD Simulations and Experiments. *Acta Mater.* 151, 191–200. doi:10.1016/j.actamat.2018.03.058

Li, B., Sun, H., and Chen, C. (2014). Large Indentation Strain-Stiffening in Nanotwinned Cubic boron Nitride. *Nat. Commun.* 5, 4965. doi:10.1038/ncomms5965

Li, B., Sun, H., and Chen, C. (2016). Extreme Mechanics of Probing the Ultimate Strength of Nanotwinned Diamond. *Phys. Rev. Lett.* 117, 116103. doi:10.1103/physrevlett.117.116103

Li, J., Fang, Q., Liu, B., and Liu, Y. (2018). Transformation Induced Softening and Plasticity in High Entropy Alloys. *Acta Mater.* 147, 35–41. doi:10.1016/j.actamat.2018.01.002

Luo, D., Zhou, Q., Ye, W., Ren, Y., Greiner, C., He, Y., et al. (2021). Design and Characterization of Self-Lubricating Refractory High Entropy Alloy-Based Multilayered Films. *ACS Appl. Mater. Inter.* 13, 55712–55725. doi:10.1021/acsami.1c16949

Matsukawa, Y., Osetsky, Y. N., Stoller, R. E., and Zinkle, S. J. (2005). The Collapse of Stacking-Fault Tetrahedra by Interaction with Gliding Dislocations. *Mater. Sci. Eng. A* 400-401, 366–369. doi:10.1016/j.msea.2005.01.063

McMurtrey, M. D., Was, G. S., Cui, B., Robertson, I., Smith, L., and Farkas, D. (2014). Strain Localization at Dislocation Channel-Grain Boundary Intersections in Irradiated Stainless Steel. *Int. J. Plast.* 56, 219–231. doi:10.1016/j.ijplas.2014.01.001

Okamoto, N. L., Fujimoto, S., Kambara, Y., Kawamura, M., Chen, Z. M. T., Matsunoshita, H., et al. (2016). Size Effect, Critical Resolved Shear Stress, Stacking Fault Energy, and Solid Solution Strengthening in the CrMnFeCoNi High-Entropy alloy. *Sci. Rep.* 6, 35863. doi:10.1038/srep35863

Peng, J., Li, L., Li, F., Liu, B., Zherebtsov, S., Fang, Q., et al. (2021). The Predicted Rate-dependent Deformation Behaviour and Multistage Strain Hardening in a Model Heterostructured Body-Centered Cubic High Entropy alloy. *Int. J. Plast.* 145, 103073. doi:10.1016/j.ijplas.2021.103073

Plimpton, S. (1995). Fast Parallel Algorithms for Short-Range Molecular Dynamics. *J. Comput. Phys.* 117, 1–19. doi:10.1006/jcph.1995.1039

Rapaport, D. C. (1999). Molecular Dynamics Simulation. *Comput. Sci. Eng.* 1, 70–71. doi:10.1109/5992.743625

Ren, S. W., Li, L., Fang, Q. H., and Li, J. (2021). Modeling and Analysis of Yielding and Strain Hardening in Metastable High-Entropy Alloys. *Phys. Status Solidi B.* 258, 2100247. doi:10.1002/pssb.202100247

Robach, J. S., Robertson, I. M., Wirth, B. D., and Arsenlis, A. (2003). *In-situ* Transmission Electron Microscopy Observations and Molecular Dynamics Simulations of Dislocation-Defect Interactions in Ion-Irradiated Copper. *Philos. Mag.* 83, 955–967. doi:10.1080/0141861031000065329

Scattergood, R. O., and Bacon, D. J. (1975). The Orowan Mechanism in Anisotropic Crystals. *Philos. Mag.* 31, 179–198. doi:10.1080/14786437508229295

Schäublin, R., Yao, Z., Baluc, N., and Victoria, M. (2006). Irradiation-induced Stacking Fault Tetrahedra in Fcc Metals. *Philos. Mag.* 85, 769–777. doi:10.1080/14786430412331319929

Silcox, J., and Hirsch, P. B. (1959a). Direct Observations of Defects in Quenched Gold. *Philos. Mag.* 4, 72–89. doi:10.1080/14786435908238228

Silcox, J., and Hirsch, P. B. (1959b). Dislocation Loops in Neutron-Irradiated Copper. *Philos. Mag.* 4, 1356–1374. doi:10.1080/14786435908233371

Singh, B. N., Golubov, S. I., Trinkaus, H., Edwards, D. J., and Eldrup, M. (2004). Review: Evolution of Stacking Fault Tetrahedra and its Role in Defect Accumulation under cascade Damage Conditions. *J. Nucl. Mater.* 328, 77–87. doi:10.1016/j.jnucmat.2004.05.001

Stukowski, A., and Albe, K. (2010). Dislocation Detection Algorithm for Atomistic Simulations. *Model. Simul. Mater. Sci. Eng.* 18, 025016. doi:10.1088/0965-0393/18/2/025016

Stukowski, A. (2010). Visualization and Analysis of Atomistic Simulation Data with OVITO-The Open Visualization Tool. *Model. Simul. Mater. Sci. Eng.* 18, 015012. doi:10.1088/0965-0393/18/1/015012

Tsuzuki, H., Branicio, P. S., and Rino, J. P. (2007). Structural Characterization of Deformed Crystals by Analysis of Common Atomic Neighborhood. *Comput. Phys. Commun.* 177, 518–523. doi:10.1016/j.cpc.2007.05.018

Wang, H., Xu, D. S., Yang, R., and Veyssière, P. (2011a). The Formation of Stacking Fault Tetrahedra in Al and CuI. Dipole Annihilation and the Nucleation Stage. *Acta Mater.* 59, 1–9. doi:10.1016/j.actamat.2010.07.046

Wang, H., Xu, D. S., Yang, R., and Veyssière, P. (2011b). The Formation of Stacking Fault Tetrahedra in Al and CuIII. Growth by Expanding Ledges. *Acta Mater.* 59, 19–29. doi:10.1016/j.actamat.2010.07.045

Wang, H., Xu, D. S., Yang, R., and Veyssière, P. (2011c). The Formation of Stacking Fault Tetrahedra in Al and CuII. SFT Growth by Successive Absorption of Vacancies Generated by Dipole Annihilation. *Acta Mater.* 59, 10–18. doi:10.1016/j.actamat.2010.07.044

Wang, H., Chen, D., An, X., Zhang, Y., Sun, S., Tian, Y., et al. (2021). Deformation-induced Crystalline-To-Amorphous Phase Transformation in a CrMnFeCoNi High-Entropy alloy. *Sci. Adv.* 7, eabe3105. doi:10.1126/sciadv.abe3105

Weng, S., Yue, X., Fu, T., Chen, X., Long, X., and Peng, X. (2020). Incipient Plasticity and Dislocation Loop Evolution in Rock-Salt Vanadium Nitride. *Ceramics Int.* 46, 11169–11178. doi:10.1016/j.ceramint.2020.01.138

Weng, S., Fang, Z., Zhao, Y., Fu, T., and Peng, X. (2021). Molecular Dynamics Studies on Size Effects in Laminated Polycrystalline Graphene/Copper Composites: Implications for Mechanical Behavior. *ACS Appl. Nano Mater.* 4, 12289–12299. doi:10.1021/acsanm.1c02778

Wu, L., Yu, W., Hu, S., and Shen, S. (2017). Stability of Stacking Fault Tetrahedron in Twin Boundary Bicrystal Copper under Shear. *Int. J. Plast.* 97, 246–258. doi:10.1016/j.ijplas.2017.06.005

Wu, L., Yu, W., Hu, S., and Shen, S. (2018a). Radiation Response of Nanotwinned Cu under Multiple-Collision Cascades. *J. Nucl. Mater.* 505, 183–192. doi:10.1016/j.jnucmat.2018.04.020

Wu, L., Yu, W., Hu, S., and Shen, S. (2018b). Shear Response of Grain Boundary Bicrystals with a Stacking Fault Tetrahedron. *Comput. Mater. Sci.* 147, 137–144. doi:10.1016/j.commatsci.2018.02.010

Wu, L., Yu, W., Hu, S., and Shen, S. (2018c). Size-dependent Stability of Stacking Fault Tetrahedron in Coherent Twin Boundary Bicrystal: Comparisons Among Al, Ni, Cu and Ag. *Comput. Mater. Sci.* 155, 256–265. doi:10.1016/j.commatsci.2018.08.049

Yadav, S. K., Liu, X.-Y., Wang, J., Ramprasad, R., Misra, A., and Hoagland, R. G. (2014). First-principles Density Functional Theory Study of Generalized Stacking Faults in TiN and MgO. *Philos. Mag.* 94, 464–475. doi:10.1080/14786435.2013.856525

Yang, B., Peng, X., Huang, C., Wang, Z., Yin, D., and Fu, T. (2019). Strengthening and Toughening by Partial Slip in Nanotwinned diamond. *Carbon* 150, 1–7. doi:10.1016/j.carbon.2019.04.107

Zhang, L., Lu, C., Michal, G., Deng, G., and Tieu, K. (2017a). The Formation and Destruction of Stacking Fault Tetrahedron in Fcc Metals: A Molecular Dynamics Study. *Scr. Mater.* 136, 78–82. doi:10.1016/j.scriptamat.2017.04.019

Zhang, L., Lu, C., Tieu, K., Su, L., Zhao, X., and Pei, L. (2017b). Stacking Fault Tetrahedron Induced Plasticity in Copper Single crystal. *Mater. Sci. Eng. A* 680, 27–38. doi:10.1016/j.msea.2016.10.034

Zhang, L., Lu, C., Tieu, K., and Shibuta, Y. (2018). Dynamic Interaction between Grain Boundary and Stacking Fault Tetrahedron. *Scr. Mater.* 144, 78–83. doi:10.1016/j.scriptamat.2017.09.027

Zhao, S., Stocks, G. M., and Zhang, Y. (2017). Stacking Fault Energies of Face-Centered Cubic Concentrated Solid Solution Alloys. *Acta Mater.* 134, 334–345. doi:10.1016/j.actamat.2017.05.001

Zhou, X.-Y., Wu, H.-H., Zhu, J.-H., Li, B., and Wu, Y. (2021). Plastic Deformation Mechanism in crystal-glass High Entropy alloy Composites Studied via Molecular Dynamics Simulations. *Compos. Commun.* 24, 100658. doi:10.1016/j.coco.2021.100658

Zhu, B., Huang, M., and Li, Z. (2017). Atomic Level Simulations of Interaction between Edge Dislocations and Irradiation Induced Ellipsoidal Voids in Alpha-Iron. *Nucl. Instr. Methods Phys. Res. Section B: Beam Interactions Mater. Atoms* 397, 51–61. doi:10.1016/j.nimb.2017.02.048

Conflict of Interest: The authors declare that the research was conducted in the absence of any commercial or financial relationships that could be construed as a potential conflict of interest.

Publisher's Note: All claims expressed in this article are solely those of the authors and do not necessarily represent those of their affiliated organizations, or those of the publisher, the editors and the reviewers. Any product that may be evaluated in this article, or claim that may be made by its manufacturer, is not guaranteed or endorsed by the publisher.